JOURNAL OF SYNCHROTRON RADIATION

ISSN 1600-5775

Received 9 February 2015
Accepted 20 April 2015

Edited by J. F. van der Veen

Keywords: photoemission microscopy; XPEEM; STXM; X-ray microscopy; synchrotron beamline; beamline design; monochromator; soft X-ray optics.

HERMES: a soft X-ray beamline dedicated to X-ray microscopy

Rachid Belkhou,* Stefan Stanescu, Sufal Swaraj, Adrien Besson, Milena Ledoux, Mahdi Hajlaoui and Didier Dalle

Synchrotron SOLEIL, L'Orme des Merisiers, Saint-Aubin, BP 48, 91192 Gif-sur-Yvette Cedex, France.
*Correspondence e-mail: belkhou@synchrotron-soleil.fr

The HERMES beamline (High Efficiency and Resolution beamline dedicated to X-ray Microscopy and Electron Spectroscopy), built at Synchrotron SOLEIL (Saint-Auban, France), is dedicated to soft X-ray microscopy. The beamline combines two complementary microscopy methods: XPEEM (X-ray Photo Emitted Electron Microscopy) and STXM (Scanning Transmission X-ray Microscopy) with an aim to reach spatial resolution below 20 nm and to fully exploit the local spectroscopic capabilities of the two microscopes. The availability of the two methods within the same beamline enables the users to select the appropriate approach to study their specific case in terms of sample environment, spectroscopy methods, probing depth *etc*. In this paper a general description of the beamline and its design are presented. The performance and specifications of the beamline will be reviewed in detail. Moreover, the article is aiming to demonstrate how the beamline performances have been specifically optimized to fulfill the specific requirements of a soft X-ray microscopy beamline in terms of flux, resolution, beam size *etc*. Special attention has been dedicated to overcome some limiting and hindering problems that are usually encountered on soft X-ray beamlines such as carbon contamination, thermal stability and spectral purity.

1. Introduction

There is a tremendous and growing need to explore detailed structural, morphological, magnetic, electronic and chemical properties of heterogeneous matter at the nanometer scale. This is almost true in all fields of science such as material and nanoscience, biology and medicine, chemistry, earth and environmental science *etc*. In turn, the advent of ultra-bright third-generation synchrotron radiation sources has opened the route to X-ray microscopy and imaging with resolution in the 10 nm ranges (Chao *et al.*, 2005; Tromp *et al.*, 2013; Schmidt *et al.*, 2005, 2013; Taniuchi *et al.*, 2015). In particular, soft X-ray microscopy is probably among the most suitable methods to respond to that demand. Beside taking advantage of the unique properties of synchrotron X-rays (tunability, high flux, polarization *etc*.), it allows spectroscopic and microscopic methods to be suitably combined. Experimentally there are two different approaches. The first uses a well focused X-ray photon beam which is scanned across the sample's surface. The second employs parallel imaging techniques making use of low-energy electron optics.

The originality of the HERMES beamline is to combine these two approaches on the same beamline with the goal to reach spatial resolution below 20 nm: STXM (scanning transmission X-ray microscopy) (Kirz & Rarback, 1985; Ade *et al.*, 1992) and XPEEM (X-ray photo-emitted electron microscopy) (Schmidt *et al.*, 1998; Locatelli & Bauer, 2008).

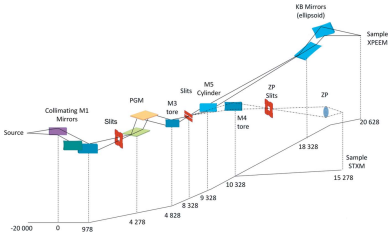

This original approach will offer two complementary microscopy techniques to the users community. On one hand XPEEM is photon-electron based and is intrinsically a surface–interface microscopy method with an ultrahigh-vacuum sample environment. On the other hand, STXM is a photon-in/photon-out based microscopy that allows to essentially investigate 'bulk' properties of materials with a more versatile sample environment.

The combination of these two microscopies opens up the scientific case of the beamline, which covers a broad range of scientific topics such as nanoscience, magnetic materials, soft matter, biology *etc.* The specifications of the beamline have been therefore optimized to fulfill the technical requirements of all the scientific areas covered by the beamline, in terms of energy range and resolution, spatial resolution, photon flux, beam size *etc.*

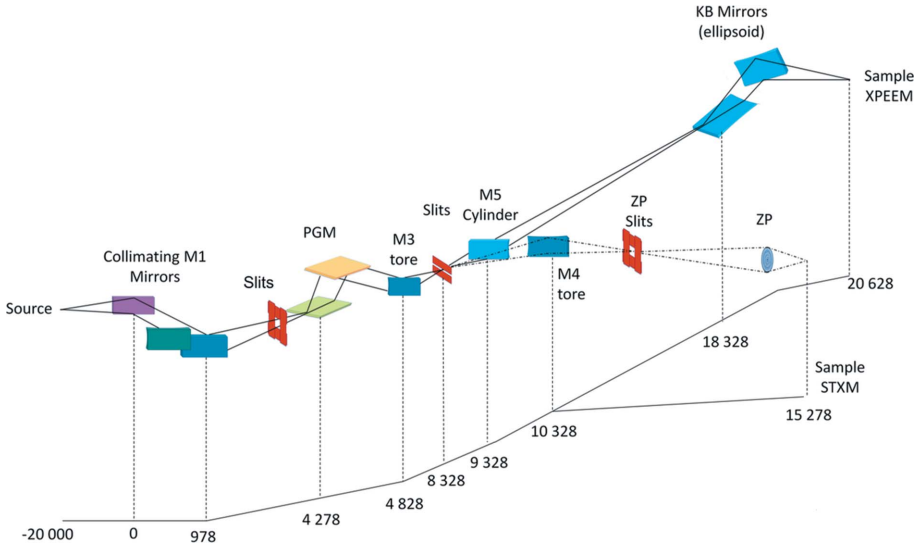

Figure 1
Optical layout of the HERMES beamline. The beamline is split into four parts: the source, which includes the two undulators (HU42, HU64); the three first mirrors (M1A, M1B, M1C) installed on a lead-shielded hutch; the monochromator hutch, in which is installed the entrance and the exit slits, the monochromator and the switching mirrors (M4, M5); the beamline splits further into two branches in the experimental hutch, where the two end-stations (XPEEM, STXM) are located

In this paper, we review in detail the measured specifications of the HERMES beamline from the source down to the monochromator. The specifications and the description of the two branches, along with the associated XPEEM and STXM microscopes, will be the subject of specific publications.

2. Beamline design

Fig. 1 shows a sketch of the beamline design starting from the source to the end-stations, including the optical elements and the photon path through the beamline.

Two APPLE-II undulators (HU42, HU64) are installed on the mid straight section I10-M of the Synchrotron SOLEIL storage ring and they cover the 70 eV to 2.5 keV photon energy range. The first optical element on the beamline is composed of a set of three mirrors in chicane configuration (M1A, M1B and M1C). M1A is a plane mirror, M1B and M1C are toroidal. The mirrors work in couples: M1A–M1B, with an incidence angle of 2.5°, are optimized for the low-energy range (<800 eV) and HU64 undulator. M1A–M1C, with an incidence angle of 1.2°, are optimized for the high-energy range (>800 eV) and HU42 undulator.

The monochromator of the beamline is a plane-grating monochromator (PGM) and includes two types of gratings: a VLS–VGD for the low-energy range (70 eV to 1.6 keV) and a multilayer grating for the high-energy side (1–2.5 keV). Three types of optical elements are installed in the monochromator chamber: a set of three plane gratings, two plane mirrors and a toroidal mirror which focuses the beam in both directions on the exit slit.

Downstream of the monochromator exit slit, a set of two mirrors are placed in order to deflect the beam towards each end-station. A cylindrical mirror (M5) deflects the beam towards the XPEEM branch; meanwhile a toroidal mirror (M4) placed 1 m further downstream deflects the beam towards the STXM branch. After these two mirrors, the beamline splits into two branches which can operate alternatively and independently. On the XPEEM branch, a set of Kirkpatrick–Baez (KB) (Kirkpatrick & Baez, 1948) bendable elliptical mirrors are placed 9 m after the M5 mirror. The KB mirrors enable focusing the beam in two independent directions down to a few micrometers. The XPEEM microscope is placed at the best focal point of the KB mirrors in order to optimize the photon density and the illumination of the field of view (FOV) of the microscope. For the STXM branch, mirror M4 focuses the beam onto a set of slits (installed 1 m further downstream) acting as a source of the zone plate (ZP) lenses of the STXM microscope.

All the optical specifications of the beamline optics are listed in Table 1.

3. Source

Two APPLE-II undulators are used to cover the large energy range required by the scientific program of the beamline. Moreover, the constraining specifications of the beamline in terms of flux ($>10^{12}$ photons s^{-1}) and of polarization rate (100% left/right circular, variable and rotatable linear) impose the use of almost exclusively the first harmonic of the undulator. In order to fulfill these requirements, the period of each undulator has been carefully chosen: HU42 for the high-energy and HU64 for the low-energy range. Fig. 2 shows the calculated photon flux for the two undulators. A detailed description of the undulators has already been published (Valleau *et al.*, 2013).

Table 1
Parameters of the optical elements of the HERMES beamline.

Optics	Shape	Substrate/ coating	Incidence (°)	Meridional/ sagittal radius (m)	Slope error (μrad)
M1A	Plane	SiC/Ni+Rh	2.5/1.2	–	0.27
M1B	Toroidal	Si/Ni	2.5	126.7/1.8	2.93
M1C	Toroidal	Si/Rh	1.2	229.5/0.887	2.05
Grating 1 450 lines mm^{-1}	VLS–VGD	Si/Ni	2.1–9.9	–	0.31
Grating 2 600 lines mm^{-1}	VLS–VGD	Si/Rh	1.9–5.2	–	0.32
Grating 3 ML	Multilayer	Si/(Cr/B_4C)	2.7–7.3	–	0.59
M2A	Plane	Si/Ni+Rh	1.2–9.9	–	0.27
M2B	Plane	Si/B_4C	1.9–6.6	–	0.59
M3	Toroidal	Si/Au	1.2	0.146/83	1.17
M4	Toroidal	Si/Au	1.35	0.0396/79	2.8
M5	Cylindrical	Si/Au	1.75	35/–	2.1
M6	Elliptical	Si/Au	1.75	Variable	0.78
M7	Elliptical	Si/Au	1.75	Variable	0.55

4. First mirrors

A set of three mirrors (M1A, M1B and M1C) are placed 20 m downstream of the center of the straight section. Since the mirrors are placed in chicane mode, the beam is shifted by 41 mm from the straight section axis in order to avoid the direct emission of unwanted radiation. A tungsten block is placed between the M1A and M1B/M1C mirrors to act as a Bremsstrahlung beam absorber. The whole M1 chamber is placed in a lead-shielded radio-protection hutch.

M1A is a plane mirror and serves primarily to deflect the beam and to absorb the large power load from the undulators. We took advantage of the low vertical emittance and the small beam footprint to adopt a multi-stripe system for M1A mirror. To optimize the mirror reflectivity, M1A received a double coating, Ni and Rh, for the low- and the high-energy range, respectively. M1B and M1C are, respectively, Ni- and Rh-coated.

Further, the toroidal mirrors M1B and M1C focus the beam horizontally 0.5 m upstream of the monochromator gratings. In the vertical direction the beam is collimated by the mirrors to obtain a parallel beam impinging the monochromator gratings. A set of slits and detectors (YAG crystal, calibrated Si diode and gold mesh) are placed between the M1 mirrors and the monochromator to optimize the pink beam before the grating.

Due to the large thermal power load that has to be absorbed by mirror M1A (up to 300 W), the characteristics of the thermal cooling have to be carefully defined. To avoid a liquid-nitrogen cooling system, SiC substrate was chosen for the M1A mirror instead of Si. Si substrate is known to dissipate large thermal loads efficiently, but not at room temperature. High-quality CVD SiC (Rohm and Haas Co.) substrate is the perfect candidate as it has been deduced from finite-element analysis. The calculations showed that, from a direct comparison of the thermal and optical performances of Si and SiC substrates, SiC is much more efficient at absorbing thermal loads below 300 W without any significant thermal deformation of the mirror. This is mainly due its higher thermal conductivity (SiC: 300 W m^{-1} K^{-1}; Si: 148 W m^{-1} K^{-1}) which allows the thermal power load to dissipate more efficiently. As M1A absorbs a large part of the incoming power load, the M1B and M1C mirrors absorb less than 10 W. Therefore, Si substrate was used for the two mirrors with only water cooling.

Experimentally, and in order to avoid thermal influence on the beam properties, a thorough investigation for the most suitable cooling temperature for the M1A mirror was performed. To accomplish this, two procedures have been followed. The aim was to determine the best M1A temperature that does not affect the optical properties of mirror M1A in terms of sagittal and meridional radius of curvature, slope errors, roughness *etc.* Ray-tracing calculations have shown that any deformation of mirror M1A due to the temperature and/or thermal load will strongly affect the beam intensity and size at the focal point. The calculations showed that the radius of curvature of M1A has to be kept above 10 km to avoid adverse effects on the beam properties.

At first, the M1A temperature was tuned using an externally controlled thermal bath varying the total X-ray power load and density. This has been achieved by moving the undulator gap forth and back from its minimum value (15.5 mm, maximum power load) to its maximum working value (50 mm, minimum power load). After each gap change, the mirrors were allowed to stabilize for 1 h and the beam size, position and intensity were monitored. This operation was repeated for various cooling temperatures from 268 K to 308 K. Surprisingly, the ideal temperature was found at 305 K. At this cooling temperature the beam size, intensity and position are not sensitive to any change in the thermal power load. The same procedure has been repeated by varying only

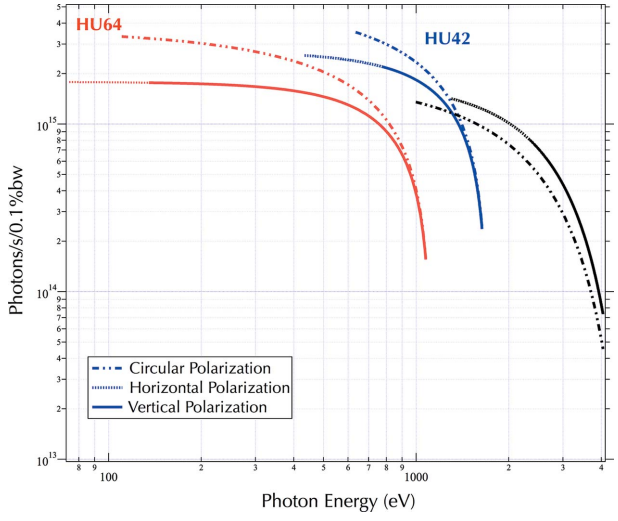

Figure 2
Calculated flux for the HU42 [first harmonic (blue), third harmonic (black)] and HU64 (red) undulators. The calculations have been made for a diaphragm opening of 2 mm × 2 mm. The diaphragm is placed 10 m downstream of the middle of the straight section. The SOLEIL machine current was set to 500 mA and beam energy to 2.75 GeV.

the total power load. For this experiment, the undulator has been kept constant (minimum gap) and the beamline diaphragm has been varied from its minimum to its maximum opening (0.1 mm to 2.5 mm). Here again we found out that a cooling temperature of 305 K is the most suitable for dissipating the power load without any degradation of the beam properties.

Even though the temperature found may seem surprising and not intuitive at first sight, it can be easily understood. High-quality SiC substrates are known to dissipate efficiently large thermal loads around room temperature (RT). However, it is also known from the SiC Young's modulus that, at around RT, a small temperature variation can induce large substrate deformations. As only a small area of the SiC is illuminated by the X-rays, a large temperature gradient can be observed across the substrate width. Therefore, the key point is to reduce the gradient temperature induced by the X-ray's power load. As a matter of fact, when M1A is exposed to the maximum X-ray power load, a large temperature gradient has been measured across the mirror's width. The lowest is the cooling temperature, the highest is the gradient. Meanwhile, close to the beam footprint on M1A, the temperature can rise up to 303–307 K. Therefore, keeping the whole M1A mirror temperature around 305 K limits the gradient effect and thus the SiC deformation. Finally, the optimum cooling temperature obtained is not high enough to induce any deterioration of the mirror properties (inter-mixing, coating peeling, roughness *etc.*).

5. Monochromator

Although the HERMES beamline is not specifically intended for high-resolution spectroscopy, high energy resolution is still required and mandatory. At first sight, it might be tempting to consider that, for performing imaging, the energy resolution can be relaxed in order to improve the photon flux. However, this simplistic view is not true for both the XPEEM and STXM microscope end-stations. In the case of the XPEEM microscope, for example, the photon beam has to match the FOV of the microscope. When seeking high photon flux, the energy slit cannot be simply opened to gain flux at the cost of energy resolution, because all the extra photons will simply fall out of the FOV of the XPEEM and therefore will not contribute to the image intensity. In turn, when looking for high energy resolution, the energy slit cannot be simply closed because the resulting beam spot on the microscope will be much smaller than the FOV and consequently the illumination will not be homogeneous. In the case of STXM, the microscope resolution will be mainly limited by the coherent part of the beam which illuminates the ZP lens. Here, again and for the entire photon energy range, the opening of the energy slit has to be suitably adjusted for an optimum ZP efficiency. Therefore, the monochromator design has to enable adjusting the beam size, energy resolution and flux simultaneously.

To fulfill these requirements, we have developed a variable-deviation PGM (Petersen, 1982; Follath, 2001) with variable line spacing (VLS) and variable groove depth (VGD) (Lagarde *et al.*, 2013*a*). The monochromator operates in the so-called Petersen mode. This means that the deviation angle, and therefore the dispersion law, can be varied by choosing a C factor from 0.2 to 0.8. The C factor is defined as $(\sin\alpha/\sin\beta)$, where α is the incidence angle on the grating and β the emergence angle. It is worth noting that, due to our specific geometry (mirror M2 is placed downstream of the grating), the deviation factor C is defined as the inverse of the C_{ff} factor introduced by Peterssen *et al*. The deviation angle Δ is then defined as $(\alpha + \beta)$. A constant C factor is the condition for a fixed focus with a plane grating in non-parallel illumination. The choice of C determines the grating angular dispersion and hence the balance between flux and resolution.

The Petersen mode enables the opening of the slit to be chosen that is most suitable for the illumination of the microscopes with respect to the photon energy, to achieve the requested energy and spatial resolution. The VLS system allows the chromatic aberration of the monochromator to be reduced; meanwhile, the VGD enables the contribution of higher order harmonics to be reduced and hence to gain in spectral purity. Two gratings (450 and 600 lines mm^{-1}) are installed to cover the photon energy range from 70 eV to 1.6 keV. For higher energy, the VLS–VGD gratings are no longer efficient. In this high-energy range, a newly developed multilayer grating (Lagarde *et al.*, 2013*b*; Choueikani *et al.*, 2013) is used to cover the 1 keV to 2.5 keV photon energy range efficiently.

In order to fulfill the scientific specifications of the beamline, a minimum of 5000 resolving power is required for the entire energy range. The ray-tracing calculations, made using the electromagnetic propagation code *CARPEM* (Mirone *et al.*, 1998), demonstrated that the monochromator is capable of achieving an ultimate resolving power (for a narrow opening of the exit slit) up to 15000. For the standard opening of the exit slit (20–50 µm), a resolving power of 7000 can be achieved for the entire energy range.

The monochromator has been constructed in collaboration with BESTEC GmbH. A set of three optical elements are used. The first optical element that receives the 'pink beam' is the grating. Three gratings are used: two VLS–VGD gratings (G1: 450 lines mm^{-1}, Ni-coated; G2: 600 lines mm^{-1}, Rh-coated) and a multilayer grating (G3: Cr/B_4C, 4 nm period). Two plane mirrors are installed downstream to deflect the beam through the optical axis of the beamline. The first mirror has a double coating: Ni for the low-energy range (<800 eV) and Rh for the high-energy range (>800 eV). The multiple stripes and coating allow the optimization of the photon reflectivity for each energy range. The second mirror is a multilayer mirror made with exactly the same elements and period as the multilayer grating (Cr/B_4C, 4 nm period). At this stage only the VLS–VGD gratings are installed. The installation and the commissioning of the multilayer grating will be the subject of a different specific publication. Finally, a toroidal mirror (M3) with a gold coating is placed downstream of the plane mirrors. It focuses the beam horizontally and vertically on the exit slit. The beam is therefore stigmatic after the energy slit.

The energy calibration and resolution measurements were carried out using a home-made ionization chamber, with an aperture of 5 mm × 5 mm and active length of about 10 cm. The chamber was separated from the beamline by differential pumping and thin aluminium foil mounted on a valve. The energy scans were recorded with a typical dwell time of 500 ms and with a gas partial pressure in the 10^{-3} mbar range. The gas absorption spectra can be collected either in total electron yield (TEY) or in total ion yield (TIY) mode. Simultaneously, the intensity of the photon transmitted through the gas cell can be collected with a photodiode.

Several standard gas-phase absorption spectra are commonly used to assess the energy resolution of soft X-ray monochromators. For our purpose, three gas absorption edges have been used: Ar 2*p* at 240 eV, N 1*s* at 401 eV and Ne 2*p* at 864 eV. Therefore, we have access to an exhaustive calibration of the energy resolution over a large energy scale using various configurations of the beamline (undulator, M1 mirrors, grating, mirror coating *etc.*).

Fig. 3 shows typical absorption spectra recorded in TIY mode. It is worth noting that without any fitting procedure it is clear from the raw data that the beamline resolution is good enough to resolve higher-order resonances for all the measured spectra. Further, for a quick estimation of the resolution, the absorption spectra have been fitted using a symmetric Voigt function which is the result of the convolution of Lorentzian and Gaussian functions. The Lorentzian width represents the natural intrinsic line-width and the Gaussian width corresponds to the energy-resolution broadening. For nitrogen, the whole spectra have been fitted because the peaks are not separated enough. For argon and neon, we focus the fitting procedure only on the $2p_{3/2}$–4*s* and 1*s*–3*p* single-peak resonances, respectively.

To estimate the energy resolution, a very accurate evaluation of the Lorentzian width is mandatory. Unfortunately, the large diverging data found in the literature may induce large errors in the resolution measurements. Although the Lorentzian width is intrinsic, we do believe that the experimental conditions of the measurements are important and can affect the energy-resolution measurements (saturation effects, non-linearity problems *etc.*). Therefore, and in our opinion, the diverging data for the estimation of the natural width of the spectra are mainly due to experimental conditions than to the fitting procedure.

To avoid this limitation we proceed following two steps. At first, N 1*s* spectra were measured under the most constraining conditions to reach the ultimate resolution of the beamline. The energy slit was set almost closed (5 µm) and the deviation angle factor was set to the minimum (C = 0.2). From the recorded spectra, the energy resolution was evaluated without any fitting process following the methods developed by Chen & Sette (1989). The energy resolution was estimated by comparing the experimental intensity ratio between the first minimum and third maximum (see Fig. 3*b*) with that from a simulated spectrum. The simulated spectrum has been obtained by convoluting a Lorentzian and a Gaussian function. The FWHM of the Gaussian have been varied from 20 meV to 150 meV. Therefore, the first minimum to third maximum ratio does not depend on the Lorentzian width estimation. From the evolution of the peaks ratio *versus* the energy resolution, the experimental resolution can be directly accessed without any further fitting procedure. For the best resolution, a ratio of 0.68 was measured which corresponds

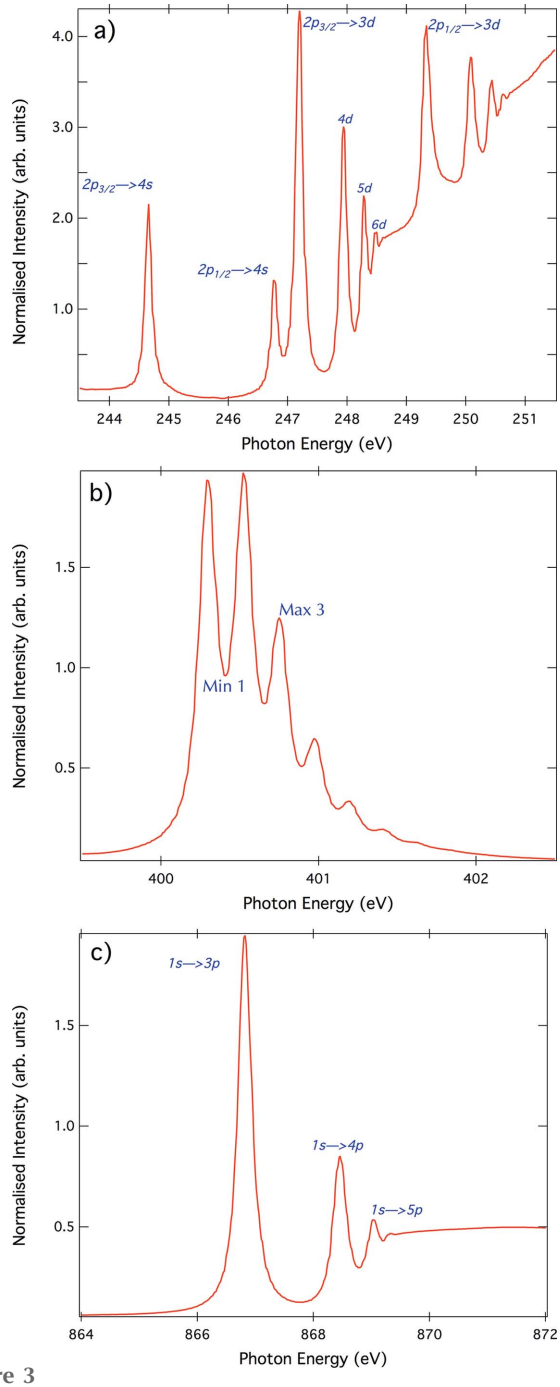

Figure 3
Typical absorption spectra recorded to evaluate the energy calibration and resolution. (*a*) Argon resonance absorption spectrum measured at the Ar $L_{2,3}$-edge. The final-state assignments are labeled. (*b*) Nitrogen $1s \rightarrow \pi^*$ resonance absorption spectrum measured at the N *K*-edge. Its fine structure is due to vibrational levels of the state. Min 1 and Max 3 refer to the intensities used to estimate the resolution without the fitting procedure as explained in the text. (*c*) Neon 1*s*–*np* resonance absorption spectrum measured at the Ne *K*-edge.

to 36 meV resolution. This procedure is the most accurate because it is not subject to errors due to an incorrect estimation of the natural line width and/or the fitting procedure. Finally, in order to verify the accuracy of the method, the Gaussian FWHMs extracted experimentally have been used to fit the N 1*s* spectrum varying the Lorentzian width. We obtain a Lorentzian width of 120 meV which is in agreement with previous results (Hitchcock & Brion, 1980; Quaresima *et al.*, 1995; Prince *et al.*, 1998; Strocov *et al.*, 2010).

Fig. 4 shows a typical fit for the absorption spectrum of N_2 at the $1s \rightarrow \pi^*$ resonance. The spectrum was recorded with the HU64 undulator, 450 lines mm^{-1} grating and a deviation factor $C = 0.2$. The slit opening was set to 10 µm.

For argon and neon gases, the Gaussian width can be confidently extracted following a consistent fitting procedure due to the presence of only one component in the recorded spectra. Here, again, the value of the width of the Lorentzian has been determined by fitting the experimental spectra obtained under the most constraining conditions for the resolution, *i.e.* slit closed at 5 µm and deviation *C* factor set at 0.2. For the Ar 2*p*–4*s* and Ne 1*s*–3*p* resonance spectra, a Voigt shape line with a Lorentzian width of 115 meV and 250 meV, respectively, have been obtained. Both values are in agreement with the reported values in the literature (King & Read, 1985; Quaresima *et al.*, 1995; Prince *et al.*, 1998; Sairanen *et al.*, 1996; Strocov *et al.*, 2010; Domke *et al.*, 1991). The three Lorentzian widths determined for the three gases here were kept constant for all the measurements.

It is worth stressing here that the exact measurement of the resolution is accurate only when the energy resolution is higher than the Lorentzian width. At the N 1*s* absorption, for example, the best resolution that can be confidently assessed is around 40 meV.

Finally, the exact position of the exit slit along the beam path has been determined by measuring the waist of the M3 mirror. The M3 mirror focuses the beam in both directions onto the exit slits. In the vertical direction the focal point of the M3 mirror, and therefore the optimum position for the energy slits, is determined by the largest energy dispersion within the exit slit (best resolution). The exit slit position has been scanned within ±100 mm along the beam path to maximize the resolving power and the energy resolution.

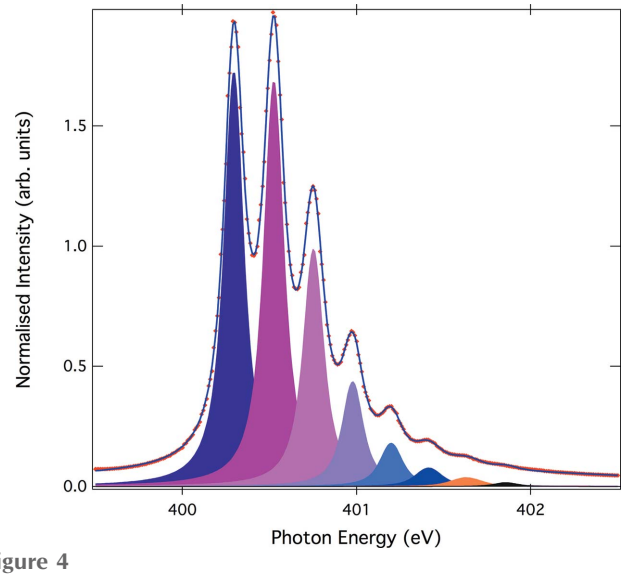

Figure 4
Fit of the N 1*s* absorption spectrum. The measured energy resolution is 36 meV. The spectrum was recorded with a slit opening of 10 µm and C = 0.2 (HU64, 450 lines mm^{-1}).

Table 2
HERMES beamline configurations and energy ranges.

Configuration	Polarization	Energy range (eV)
Low energy: HU64-G1	Linear horizontal	70–800
	Linear vertical	150–800
	Circular left/right	135–800
High energy: HU42-G2	Linear horizontal	450–1600
	Linear vertical	550–1600
	Circular left/right	800–1600

Further, the energy resolution and calibration have been characterized for all the working conditions of the beamline. Table 2 summarizes the different energy configurations of the beamline.

5.1. Low-energy configuration

In the low-energy configuration, the undulator HU64 is used in combination with mirrors M1A–M1B. Both mirrors are Ni coated and the beam is incident at 2.5°, in order to ensure a high reflectivity for low-energy range and a better high harmonic rejection. In this configuration the 450 lines mm^{-1} grating and M2 plane mirrors (Ni coated stripe) are used. The M3 mirror remains fixed for all the configurations.

To characterize the resolution in this energy range, both the Ar and N_2 gases have been used. For each *C* factor, ranging from 0.2 to 0.8, the energy resolution and the photon flux have been measured as a function of the slit opening. The smaller the *C* factor, the higher the energy dispersion, and hence the resolving power. At the Ar 2*p* resonance (∼240 eV) an ultimate resolving power of 14000 was achieved which corresponds to an energy resolution of 17 meV. For the N 1*s* resonance (∼401 eV), the ultimate resolving power is 11000 (energy resolution = 36 meV). Both values are in good agreement with the ray-tracing calculations and fulfill the specifications of the beamline.

The energy resolution and photon flux measured at the Ar 2*p* absorption energy are plotted in Fig. 5. From Fig. 5(*a*) one may clearly see that, above 20 µm, the energy resolution varies linearly with the slit opening as expected from the ray-tracing calculations. Below 20 µm, the resolution saturates irrespective of the slit opening. At this slit opening, the energy resolution is only limited by the aberrations of the monochromator, the beam size and divergence. The photon flux increases with increasing slit opening and *C* factor, but it tends to saturate for very large slit opening, as expected. The same results and behavior have been observed at the N 1*s* energy (not shown).

From Fig. 5, and as discussed above in the preamble of this section, it is quite difficult to define the optimum working

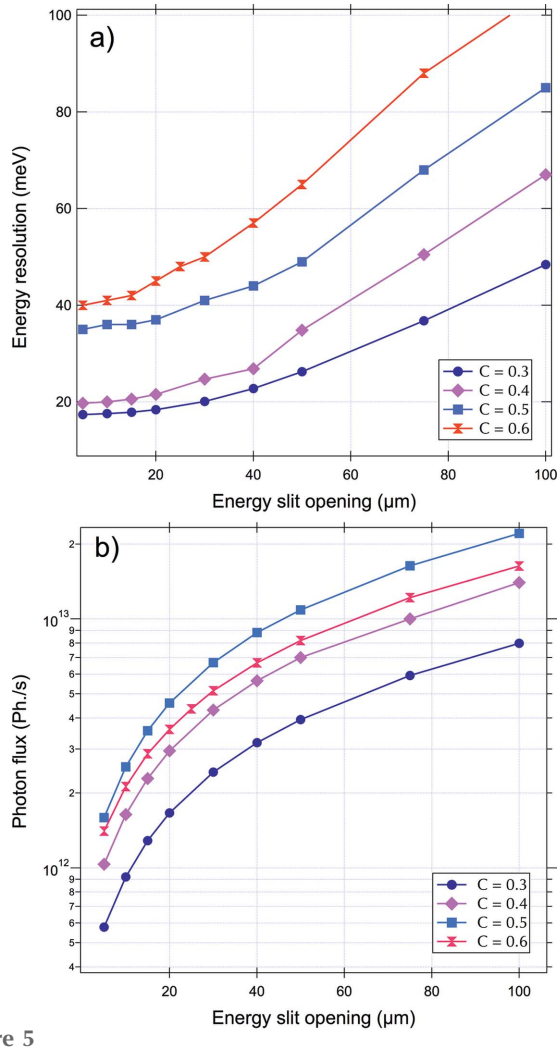

Figure 5
Measured (*a*) resolution and (*b*) flux at the Ar 2*p* resonance as a function of the energy slit opening and for selected *C* factors. The HU64 undulator and the Ni-coated 450 lines mm^{-1} G1 grating have been used for these measurements.

conditions for the microscopes. For that purpose a figure-of-merit function, *Q*, has been calculated. This formula has no physical meaning and is purely empirical. However, it enables the most pertinent factors for the beamline optimization to be easily identified. *Q* is defined as follows:

$$Q(\text{Slit}) = A\,\frac{\sqrt{\text{Flux}/10^{11}}}{\text{Resolution}}, \qquad (1)$$

where 10^{11} corresponds in our case to the minimum required photon flux per second to operate the microscopes. *A* is a normalization constant that depends on the energy. The resolution is expressed in meV. In the case of N 1*s* (400 eV, *A* = 4), *Q* will have the maximum value of 1 if we achieve simultaneously an energy resolution of 40 meV and a photon flux of 10^{13} photons s^{-1}, which correspond to our best-case scenario.

Fig. 6 shows the calculated *Q* factor in the case of the N 1*s* spectra. For STXM and XPEEM microscopes, a slit opening between 20 and 50 μm will be mainly used. From the figure, it can be clearly seen that the optimum flux and resolution are

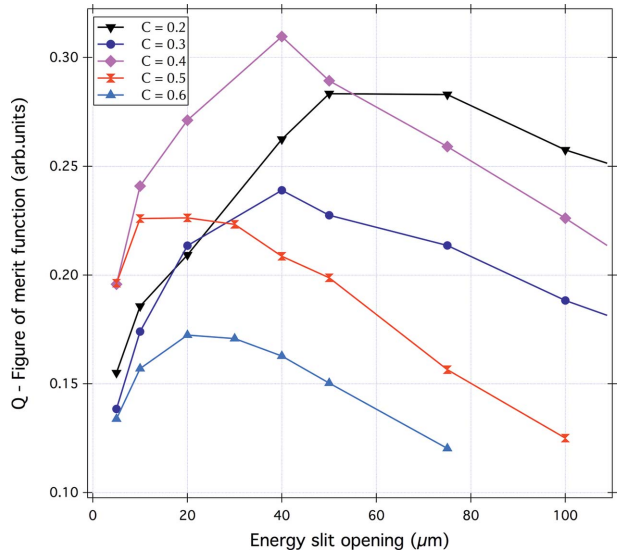

Figure 6
Figure-of-merit function (*Q*) calculated for selected *C* factors and slit openings (N 1*s* absorption edge).

obtained for C_{ff} = 0.4. For higher slit openings and large beam size on the microscopes, C_{ff} = 0.2 is more efficient.

Similar *Q* factor calculations have been made for the data obtained at the Ar 2*p* absorption energy and give rise to the same conclusions.

Finally, the same resolution and flux measurements have been performed with the vertical and circular polarized light in order to exclude any limitations from the undulator and the beam divergence.

5.2. High-energy configuration

For the high-energy range, the undulator HU42 is used in combination with M1A–M1C mirrors. Both mirrors are Rh-coated and the beam is at a much smaller grazing angle (1.2°), in order to ensure a high reflectivity at higher photon energy and to avoid any cut-off. In this configuration the 600 lines mm^{-1} grating and M2 plane mirrors (Rh-coated stripe) are used.

The energy resolution and flux measurements have been performed following the same method as described earlier. The spectra were recorded at both the N 1*s* and Ne 3*p* absorption spectra. The two HU64 and HU42 undulators, as well as the two gratings G1 and G2, overlap perfectly in linear horizontal polarization around the N 1*s* absorption edge (∼400 eV). Therefore, we have double-checked the resolution measurements in two extreme configurations. Fig. 7 shows the energy resolution measured at the Ne absorption edge and the photon flux. Here again the ultimate resolution was found to be in agreement with the calculations. At the Ne edge, a resolving power of 9500 has been achieved which corresponds to an ultimate energy resolution of 90 meV.

Similar 'figure of merit' *Q* function calculations have also been performed in this configuration and give rise to the same conclusions, *i.e.* *C* = 0.4 is the most appropriate configuration for a good illumination of the two microscopes.

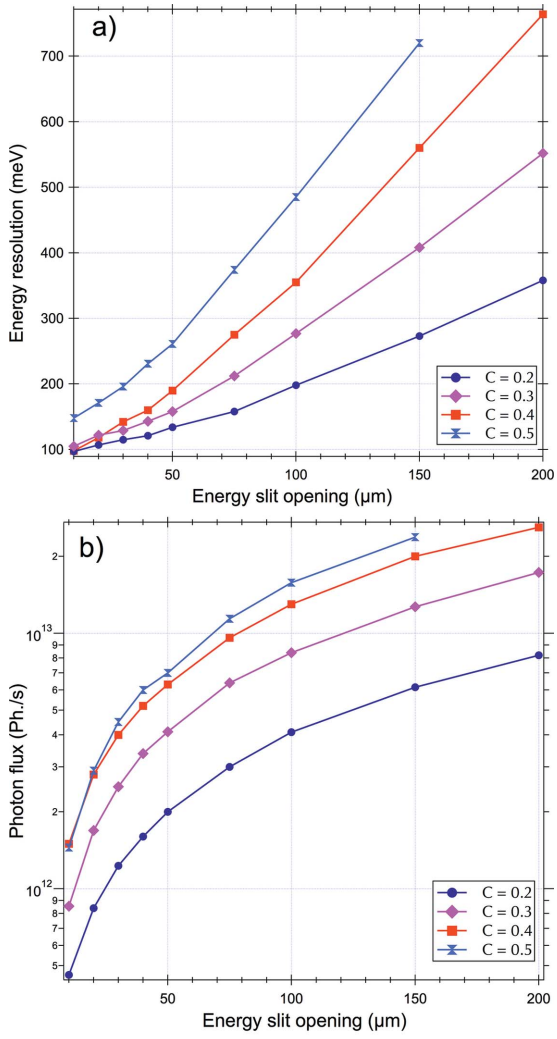

Figure 7
Measured resolution and flux at Ne 1*s* resonance as a function of the energy slit opening and for selected *C* factors. The HU42 undulator and the Rh-coated 600 lines mm^{-1} grating have been used for these measurements.

5.3. Beamline flux and energy overlapping

The photon flux over the entire energy range has been measured in gap-scan mode following only the contribution of the first undulator harmonic. The absolute flux has been measured using a calibrated photodiode placed just after the exit slit. Fig. 8 shows the photon flux distribution for three light polarizations: linear horizontal/vertical and circular left. The measurements were performed with the HU42 undulator and G2 grating. The energy slit was kept fixed at 40 μm and the *C* factor at 0.4, ensuring a minimum of 7000 resolving power over the whole scanned energy range.

From Table 2 one may see clearly that there is a perfect overlapping of the undulators and the gratings over the whole energy range, and this for all the polarizations used. The intensity difference when switching from left to right circular polarization is below 0.2% which indicates a perfect alignment and phasing of the undulators (Fig. 9). Finally, we achieve an absolute photon flux of up to 10^{13} photons s^{-1} with a minimum

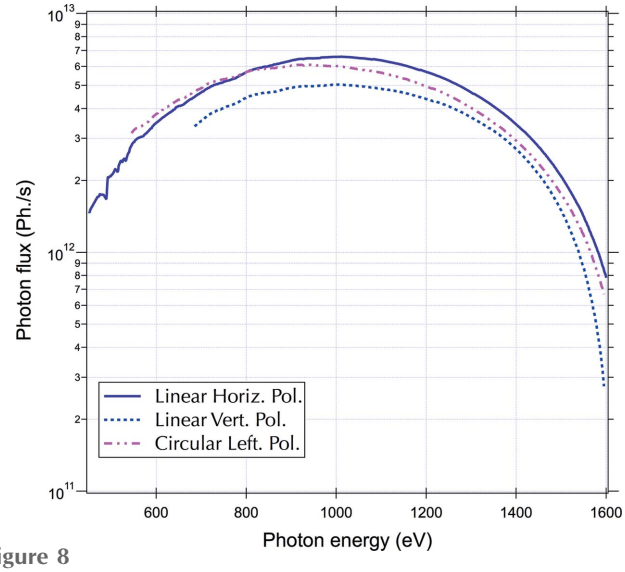

Figure 8
Measured flux for the HU42 undulator for different polarizations. The Rh-coated 600 lines mm^{-1} G2 grating has been used for these measurements with *C* set at 0.4 and a slit opening of 40 μm. This configuration enables a minimum resolving power of 7000 over the whole energy range.

of 5 × 10^{11} photons s^{-1} over the entire energy range, in agreement with the required specifications.

6. Harmonic rejection

When working at the absorption edges of low-*Z* elements and more specifically within the so-called 'water window' (280–530 eV), the spectral purity starts to be of importance and has to be significantly improved in order to ensure good spectro-microscopy measurements (Ade & Hsiao, 1993). A spectral purity in the 10^{-3} range is mandatory to fulfill the technical and scientific requirements. The spectral purity is mostly

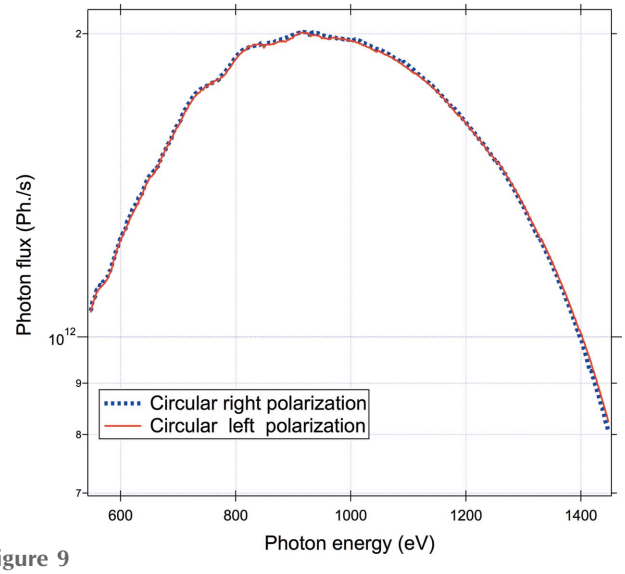

Figure 9
Direct comparison of the photon flux between circular right and left polarized light. The measurements have been performed with the undulator HU42 and the 600 lines mm^{-1} G2 grating.

limited by the high monochromator diffraction orders of high undulator harmonics. Owing to the energy range of the beamline, the most limiting is the second harmonic.

The chicane mode used in our first mirrors setup allows a large contribution of the second harmonic of the HU64 undulator to be rejected. The high incidence angle (2.5°) in double reflection on M1A–M1B enables to reduce the contribution of the second harmonic above 600 eV. The Ni coating of the mirror helps also to reduce the reflectivity above 850 eV. However, below these energies the remaining second harmonic contamination is still important and is very difficult to remove with a classical grating. Following a development made by the optics group of Synchrotron SOLEIL, the HERMES gratings have been specifically designed in order to ensure high harmonic rejection. A new concept of laminar lateral VGD has been adopted for our two gratings. The main idea here is that the groove depth is not uniform over the width of the gratings as in the case of classical gratings. Therefore, for a specific energy, we may find a groove depth that privileges the first order over the second order. A detailed description of this novel upgrade for soft X-ray monochromators can be found elsewhere (Lagarde *et al.*, 2013*a*). In the case of the 450 lines mm^{-1} grating, for example, the grating has a groove depth varying from 7.5 nm, at −18 mm from the centerline, to 43.5 nm at +18 mm. As the beam size spreads over 1 mm laterally on the grating, one can scan the beam over the whole width of the grating to find the most appropriate region for harmonic rejection.

Fig. 10 shows two N 1*s* spectra recorded with the first and second harmonic contributions. For the latter, the monochromator–undulator is scanned in order to deliver a photon energy of 200 eV at the first order. However, at this energy, the contribution of the second undulator harmonic (400 eV) is not completely rejected by the grating. Therefore, a photon energy around 400 eV (double energy) is also emitted when scanning the monochromator–undulator around 200 eV. This is why we can collect a N 1*s* spectrum with the monochromator–undulator set at half of the N 1*s* resonance energy. By measuring the total intensity of the absorption edge in the two configurations, we may therefore directly access the ratio between the first and second harmonic contributions at 200 eV. This operation is repeated while scanning the beam over the whole grating width to optimize the VGD effect.

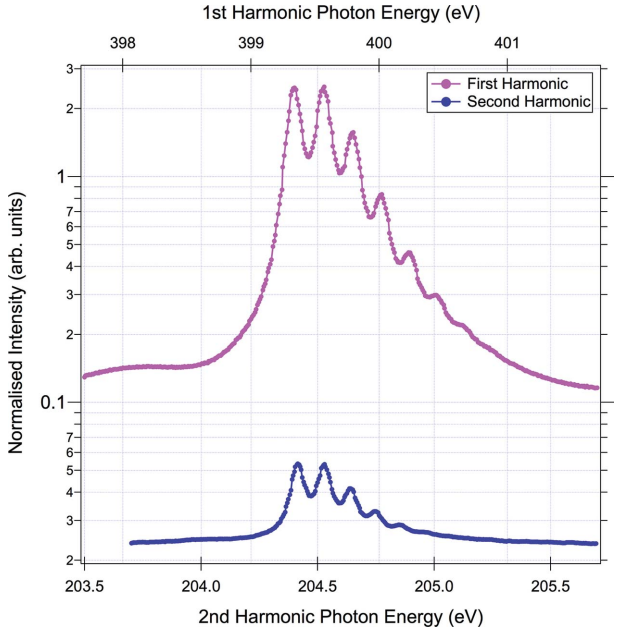

Figure 10
Effect of the VGD grating on the harmonic rejection. The bottom spectrum has been recorded with half of the resonance energy of the N 1*s* absorption edge in order to evaluate the contribution of the second harmonic contribution. The top spectrum has been taken with the first harmonic set around 400 eV. The spectra have been measured using the HU64 undulator with linear horizontal polarization.

For 200 eV energy and a *C* factor set at 0.2, we found that a groove depth of 12 nm is the most efficient to reject the second harmonic contribution. We obtain a rejection factor of 2×10^{-2}. Although we are a bit far from the specified values, the improvement of the rejection due to the VGD is of great importance. To improve the rejection down to 10^{-3}, one has to install an additional setup after the monochromator (gas filter or harmonic rejection mirrors).

Finally, it is worth noting that the procedure described here above is not the most efficient to evaluate precisely the harmonic rejection factor. Since we rely on the gas absorption edges, only a selected set of energies can be used. The efficiency and calibration of the VGD system has to be performed using photoemission spectroscopy on a known clean metal surface. Core-level photoemission allows separating the contributions of the different harmonics of the beamline since characteristic lines appear at shifted kinetic energies. These measurement will be refined further using the photo-electron spectrometer installed on the XPEEM microscope.

7. Carbon contamination

With the advent of ultra-bright third-generation synchrotron sources, carbon contamination of beamlines optical elements has become a real limiting problem (Boller *et al.*, 1983; Chauvet *et al.*, 2011). The optimization of the ultra high vacuum, the choice of carbon-free materials, the improvement of the cleaning of the mirrors coating *etc.* do not improve significantly this issue. Being aware of this limiting problem we have developed various procedures during the construction of the beamline to reduce the carbon contamination of the optics. This issue is specifically important for the HERMES beamline, since its main objective is to develop microscopy methods and tools within the water window energy range, which obviously includes the carbon 1*s* absorption energy region. Among the procedures used for reducing carbon contamination:

(i) All the optical vacuum chambers used on the beamline are exclusively made with aluminium in order to reduce a possible source of carbon when using instead stainless steel chambers. The effect of an aluminium chamber on the reduction of carbon cracking has been demonstrated since the 1980s, mainly from the cyclotron machine engineering side. As a matter of fact, Ishimaru *et al.* (Ota *et al.*, 1996; Chen, 1985*a*,*b*; Ishimaru, 1984), have demonstrated that adopting an alumi-

nium chamber reduces the desorption of carbon radicals (CH_x, CO_x, ...) during the exposure to X-rays or a synchrotron beam, by at least one order of magnitude. Moreover, it has been demonstrated that by coating the aluminium chamber with a thick Al_2O_3 film (Ishimaru, 1989; Dylla, 1993) the desorption of CH_x/CO_x radicals induced by the beam can be reduced even further. This thick oxide layer acts as a barrier to prevent any carbon desorption from the chamber walls. The oxide layer should be thick and smooth enough to cover the whole surface of the UHV chamber walls. Typically, a 300–500 nm-thick Al_2O_3 film is formed, which corresponds to the average residual roughness of the aluminium chamber. For this purpose, a specific procedure has been developed to form a thick Al_2O_3 capping layer on the walls of the aluminium vessel chambers. In brief, the chambers are baked at 453 K before the installation of any mechanical or optical components. At the end of the baking, the chamber is vented with pure oxygen and kept at this temperature for 24 h. Further, the chamber is cooled down under pure oxygen flow to RT. This procedure ensures the formation of a thick 350 nm Al_2O_3 layer capping the chamber walls.

(ii) One of the major sources of the carbon contamination in the optical chambers is the in-vacuum encoders, motors and cables. Even if these devices are specified to be UHV compatible, it is difficult to avoid the desorption of carbon radicals induced by the X-rays. Therefore, whenever possible, we have avoided the use of in-vacuum motors and encoders in most of the optical UHV chambers. Unfortunately, this is not always obvious especially when high-precision positioning is required.

(iii) Cryogenic cooling is the most efficient process to limit the effect of thermal bumps on the optics. Unfortunately, the low-temperature cooling is also responsible for an enhancement of the CHx/CO_x cracking on metallic surfaces. We have therefore avoided the use of cryo-cooling and used instead a water-cooling system with SiC substrate, as explained earlier.

(iv) Obviously, a long and careful conditioning allows the carbon contamination to be reduced. For the most critical optics such as the M1A, an almost two-month period has been dedicated for conditioning the vacuum by exposing the chamber to increasing the X-ray power load, keeping the vacuum pressure as low as possible. Moreover, we have performed all the conditioning on a 'sacrificed' area of the optics. As the beam size is very small, especially in the vertical direction, we have managed to have large optics which allows different working regions to be selected. After the conditioning, a fresh area is used for the real experiment.

(v) From a recent study, it appears that exposing the optics to a small oxygen partial pressure while using the X-ray beam reduces the carbon contamination (Risterucci *et al.*, 2012). This procedure involves a complex oxydo-reduction chemical reaction triggered by the UV–X-ray light. While the carbon radicals are cracked close to the optical surface, the presence of pure oxygen and UV–X-rays induces the formation of CO/CO_2 molecules that are in turn desorbed from the surface and pumped. This procedure is very efficient when using low-temperature cooling and has only a limited effect with RT cooling.

(vi) Once the optical mirrors are too contaminated with carbon, a cleaning procedure is required. This procedure is very well known and make uses of oxygen plasma with a UV light exposure of the optics. The procedure is very efficient but requires the removal of the optics from the UHV chamber. This can be very demanding and time-consuming as a long conditioning and alignment procedure may be required after the re-installation. Alternatively, an in-vacuum and *in situ* DC discharge UV lamp can be used.

In spite of all these precautions, it was not possible to avoid a moderate carbon contamination of the optics. We have carefully tracked the origin of this contamination and it appears that it is mainly located on the grating and mirrors of the monochromator. All the other beamline mirrors, especially the M1 first mirrors which receive the white beam and a large power load, surprisingly do not show a significant carbon contamination. Having followed the same procedures for the monochromator and the other chambers, we came to the conclusion that this carbon contamination is mainly due to the in-vacuum encoders, motors and cables. As a matter of fact, we have managed to avoid the use of in-vacuum motors and encoders in all the chambers except the monochromator. The high angular precision of the optics positioning did not allow the use of in-vacuum encoders to be avoided in the monochromator chambers. Thankfully, all the calibration, tests and commissioning have been performed on a small region of the gratings and mirrors which was sacrificed for that purpose. A clean area has been kept for the real measurements once the monochromator conditioning is completed.

Fig. 11 shows two spectra recorded on the 'sacrificed area' of the monochromator grating/mirror and on a fresh region. One can clearly see that the carbon contamination reduces the beamline flux by almost two orders of magnitude. The carbon contamination rate seems to decrease and reduce with time and after long conditioning. The small amount of carbon contamination remaining on the fresh area should not hinder the measurements at the carbon edge. Further, and if required, the monochromator optics will be cleaned using UV and oxygen plasma to remove the remaining carbon contamination.

8. Conclusions

We have presented in detail the design, technical specifications and commissioning of the HERMES beamline at the Synchrotron SOLEIL facility. Special attention has been dedicated to overcoming some limiting and hindering problems that are usually encountered on soft X-ray beamlines such as carbon contamination, thermal, stability and spectral purity.

The beamline was designed to deliver high photon flux and sufficient energy resolution to operate both STXM and XPEEM microscopes' end-stations. The beamline covers the 70–2.5 keV energy range with full polarization control, deli-

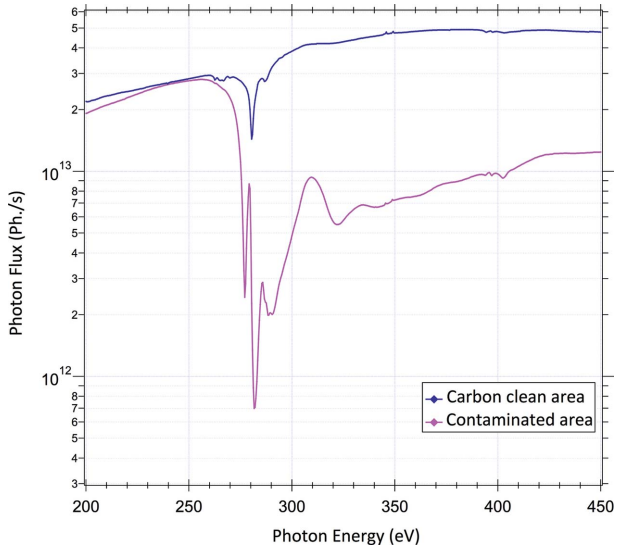

Figure 11
Effect of carbon contamination on the beamline flux. The two spectra were recorded on a 'fresh' and a 'contaminated' area. The measurements were performed in the low-energy configuration using the HU64 undulator and the 450 lines mm^{-1} G1 grating.

vering left and right circular as well as 0 to 180° rotatable linear polarization.

A PGM monochromator with variable deviation angle allows convenient optimization of the *C* factor for maximal flux or resolution. More importantly, the monochromatic beam size can be suitably adapted to meet the requirements of the microscopes in terms of illumination and beam coherence. The commissioning of the monochromator, performed using gas resonance absorption spectroscopy, shows that the beamline fulfills the required technical specifications in terms of flux and resolution. In the high-resolution mode, a resolving power up to 14000 has been demonstrated with photon flux in the 10^{12} photons s^{-1} range. In the high-flux mode, the photon flux in the 10^{13} photons s^{-1} range has been achieved at the cost of a moderate resolving power of 5000.

Thanks to the VGD concept, the spectral purity has been significantly improved to reduce the second-order harmonic contamination of the monochromatic light, down to 10^{-2}. For each photon energy, a specific groove depth of the grating can be found that allows the optimization of the first to second harmonic ratio.

Finally, since the beamline will be mainly dedicated to soft X-ray microscopy in the so-called 'water-window', special care has been taken concerning the carbon contamination problems. Several strategies have been developed in order to overcome this limitation and have enabled the carbon contamination to be kept at a manageable level.

Acknowledgements

The authors are very thankful to B. Capitano, G. Cauchon and M. Sebdaoui for their technical, scientific and logistic support during the alignment and the commissioning of the beamline. We would like also to thank B. Lagarde, T. Moreno and F. Polack for the beamline design, the ray-tracing calculations and very fruitful discussions.

References

Ade, H. & Hsiao, B. (1993). *Science*, **262**, 1427–1429.
Ade, H., Zhang, X., Cameron, S., Costello, C., Kirz, J. & Williams, S. (1992). *Science*, **258**, 972–975.
Boller, K., Haelbich, R.-P., Hogrefe, H., Jark, W. & Kunz, C. (1983). *Nucl. Instrum. Methods Phys. Res.* **208**, 273–279.
Chao, W., Harteneck, B. D., Liddle, J. A., Anderson, E. H. & Attwood, D. T. (2005). *Nature (London)*, **435**, 1210–1213.
Chauvet, C., Polack, F., Silly, M. G., Lagarde, B., Thomasset, M., Kubsky, S., Duval, J. P., Risterucci, P., Pilette, B., Yao, I., Bergeard, N. & Sirotti, F. (2011). *J. Synchrotron Rad.* **18**, 761–764.
Chen, C. T. & Sette, F. (1989). *Rev. Sci. Instrum.* **60**, 1616.
Chen, J. R. (1985*a*). *J. Vac. Sci. Technol. A*, **3**, 2200.
Chen, J. R. (1985*b*). *J. Vac. Sci. Technol. A*, **3**, 2188.
Choueikani, F., Bridou, F., Lagarde, B., Meltchakov, E., Polack, F., Mercere, P. & Delmotte, F. (2013). *Appl. Phys. A*, **111**, 191–198.
Domke, M., Xue, C., Puschmann, A., Mandel, T., Hudson, E., Shirley, D., Kaindl, G., Greene, C., Sadeghpour, H. & Petersen, H. (1991). *Phys. Rev. Lett.* **66**, 1306–1309.
Dylla, H. F. (1993). *J. Vac. Sci. Technol. A*, **11**, 2623.
Follath, R. (2001). *Nucl.Instrum. Methods Phys. Res. A*, **467–468**, 418–425.
Hitchcock, A. & Brion, C. (1980). *J. Electron Spectrosc. Relat. Phenom.* **18**, 1–21.
Ishimaru, H. (1984). *J. Vac. Sci. Technol. A*, **2**, 1170.
Ishimaru, H. (1989). *J. Vac. Sci. Technol. A*, **7**, 2439.
King, G. C. & Read, F. (1985). *Atomic Inner Shell Physics.* New York: Plenum.
Kirkpatrick, P. & Baez, A. V. (1948). *J. Opt. Soc. Am.* **38**, 766.
Kirz, J. & Rarback, H. (1985). *Rev. Sci. Instrum.* **56**, 1.
Lagarde, B., Choueikani, F., Capitanio, B., Ohresser, P., Meltchakov, E., Delmotte, F., Krumrey, M. & Polack, F. (2013*b*). *J. Phys. Conf. Ser.* **425**, 152012.
Lagarde, B., Sirotti, F., Taleb-Ibrahimi, A., Miron, C. & Polack, F. (2013*a*). *J. Phys. Conf. Ser.* **425**, 152022.
Locatelli, A. & Bauer, E. (2008). *J. Phys. Condens. Matter*, **20**, 093002.
Mirone, A., Delcamp, E., Idir, M., Cauchon, G., Polack, F., Dhez, P. & Bizeuil, C. (1998). *Appl. Opt.* **37**, 5816.
Ota, N., Kanazawa, K., Kobayashi, M. & Ishimaru, H. (1996). *J. Vac. Sci. Technol. A*, **14**, 2641–2644.
Petersen, H. (1982). *Opt. Commun.* **40**, 402–406.
Prince, K. C., Blyth, R. R., Delaunay, R., Zitnik, M., Krempasky, J., Slezak, J., Camilloni, R., Avaldi, L., Coreno, M., Stefani, G., Furlani, C., de Simone, M. & Stranges, S. (1998). *J. Synchrotron Rad.* **5**, 565–568.
Quaresima, C., Ottaviani, C., Matteucci, M., Crotti, C., Antonini, A., Capozi, M., Rinaldi, S., Luce, M., Perfetti, P., Prince, K. C., Astaldi, C., Zacchigna, M., Romanzin, L. & Savoia, A. (1995). *Nucl. Instrum. Methods Phys. Res. A*, **364**, 374–379.
Risterucci, P., Held, G., Bendounan, A., Silly, M. G., Chauvet, C., Pierucci, D., Beaulieu, N. & Sirotti, F. (2012). *J. Synchrotron Rad.* **19**, 570–573.
Sairanen, O.-P., Kivimki, A., Nmmiste, E., Aksela, H. & Aksela, S. (1996). *Phys. Rev. A*, **54**, 2834–2839.
Schmid, P., Feng, J., Padmore, H., Robin, D., Rose, H., Schlueter, R., Wan, W., Forest, E. & Wu, Y. (2005). *Rev. Sci. Instrum.* **76**, 023302.
Schmidt, T., Heun, S., Slezak, J., Diaz, J., Prince, K., Lilienkamp, G. & Bauer, E. (1998). *Surface Rev. Lett.* **5**, 1287–1296.
Schmidt, T., Sala, A., Marchetto, H., Umbach, E. & Freund, H.-J. (2013). *Ultramicroscopy*, **126**, 23–32.

Strocov, V. N., Schmitt, T., Flechsig, U., Schmidt, T., Imhof, A., Chen, Q., Raabe, J., Betemps, R., Zimoch, D., Krempasky, J., Wang, X., Grioni, M., Piazzalunga, A. & Patthey, L. (2010). *J. Synchrotron Rad.* **17**, 631–643.
Taniuchi, T., Kotani, Y. & Shin, S. (2015). *Rev. Sci. Instrum.* **86**, 023701.
Tromp, R. M., Hannon, J. B., Wan, W., Berghaus, A. & Schaff, O. (2013). *Ultramicroscopy*, **127**, 25–39.
Valleau, M., Benabderrahmane, C., Chubar, O., Marteau, F., Belkhou, R., Miron, C., Rueff, J.-P. & Couprie, M.-E. (2013). *J. Phys. Conf. Ser.* **425**, 032015.